Materials Today Bio 35 (2025) 102353

Contents lists available at ScienceDirect

Materials Today Bio

journal homepage: www.journals.elsevier.com/materials-today-bio

Glycyrrhizic acid-based nanotheranostic system to enhance photothermal immunotherapy by suppressing HSP90 and remodeling tumor microenvironment

Yihan Wu [a,1], Chenglin He [a,1], Yu Huang [a], Zhen Liu [a], Ying Zhu [a], Manyin Zhang [a], Jingjing Li [b], Yu You [a], Yitao Wang [a], Tao Chen [c], Jinming Zhang [a,*]

[a] *State Key Laboratory of Southwestern Chinese Medicine Resources, School of Pharmacy, Chengdu University of Traditional Chinese Medicine, Chengdu, China*
[b] *Department of Rehabilitation Sciences, Faculty of Health and Social Sciences, Hong Kong Polytechnic University, SAR, Hong Kong, China*
[c] *Chengdu Pidu District Hospital of Traditional Chinese Medicine, Chengdu, China*

ARTICLE INFO

Keywords:
Glycyrrhizic acid
Nanotheranostic system
IR780
Chemo-PTT
Immunochemotherapy

ABSTRACT

Anticancer photothermal therapy efficacy is currently restricted by heat shock protein (HSP90)-mediated thermoresistance, immunosuppressive microenvironment, and poor delivery efficiency of photosensitizers. At present, the “all-in-one” therapeutic system that can simultaneously achieve tumor-targeted delivery, efficient photothermal therapy, and tumor immune enhancement effects is desperately needed. We previously fabricated Glycyrrhizic acid (GL)-based lipid nanoparticles (GLPs) that possess hepatocellular carcinoma (HCC) targeting and improved membrane stability. Interestingly, GL exhibits the potential to inhibit the up-regulated HSP90 and regulate the immunosuppressive tumor microenvironment. Herein, the near-infrared photosensitizer IR780 was efficiently encapsulated into GLPs to promote photothermal enhancement and synergistic immunosuppressive anti-tumor effects. Under the irradiation of NIR light, the IR780 GLPs effectively enhance the PTT efficacy on the HCC-bearing mice model via suppressing HSP90 expression with the combination of GL. Furthermore, IR780 GLPs exhibited strong HCC targeting ability, effectively downregulating the expression of immunosuppressive Treg cells, promoting the repolarization of M2 macrophages to M1 macrophages, increasing the infiltration of cytotoxic $CD8^+$T cells and downregulating the expression of TGF-β and IL-10, upregulating IL-12, TNF-α, and IFN-γ, reshaping the tumor immunosuppressive microenvironment. Overall, we developed a novel GL-based lipid nanoparticle system encapsulating IR780 to amplify the synergistic effects of chemo-PTT for HCC treatment.

1. Introduction

Phototherapy has emerged as a promising strategy in cancer treatment, offering advantages such as non-invasiveness, minimal systemic toxicity, and precise spatiotemporal control [1,2]. Among various photosensitizers, the near-infrared (NIR) dye IR780 has attracted considerable attention due to its unique ability to integrate photodynamic therapy (PDT), photothermal therapy (PTT), and diagnostic functions, thereby effectively killing tumor cells and inhibiting tumor growth [3–6]. To enhance the tumor-targeting efficiency and photostability of IR780 in vivo, several nanocarriers have been extensively explored to enhance the delivery and therapeutic performance of IR780 in tumor treatment [7–11]. Wu et al. constructed hyaluronic acid-coated infinite coordination polymer nanoparticles loaded with IR780 and gossypol-Fe(III)-catechol, achieving 98.7% tumor inhibition via photothermal-chemotherapeutic synergy [12]. Zhao et al. developed supramolecular IR780@PT nanoparticles by conjugating IR780 with β-cyclodextrin-cisplatin complexes, demonstrating enhanced efficacy through mitochondria-targeted photothermal/photodynamic-chemotherapeutic combination [13].

However, apart from efficient delivery using nanosystems, the application of IR780-based phototherapy is also greatly hindered by the over-expression of heat shock proteins (HSPs) and tumor immunosuppressive microenvironment [14,15]. With the accumulation of photosensitizers in the body, the significantly elevated temperature may

---

[*] Corresponding author. State Key Laboratory of Southwestern Chinese Medicine Resources, School of Pharmacy, Chengdu University of Traditional Chinese Medicine, Chengdu 611137, China.

E-mail address: cdutcmzjm@126.com (J. Zhang).

[1] These authors contributed equally to the paper.

https://doi.org/10.1016/j.mtbio.2025.102353
Received 21 June 2025; Received in revised form 4 September 2025; Accepted 24 September 2025

confer collateral damage to normal tissue. Particularly, once the temperature exceeds 45 °C, the induced PTT would result in the high expression of HSP90 to cause the heat stress tolerance of cancer cells, leading to high chances of recurrence [16,17]. The nano-micelles co-delivering HSP90 inhibitor (BIIB021) and IR780 have been previously reported to obtain the mild-temperature PTT and reduce cell tolerance to heat [18]. Furthermore, the immune activation effect mediated by PDT makes the tumor immunotherapy benefits as well, which would be seriously weakened by the immunosuppressive tumor microenvironment (ITME), characterized by the accumulation of infiltrating regulatory T cells (Tregs), M2-polarized TAMs, and the up-regulation of immunosuppressive factors [19,20]. Zhang et al. developed multiple functional NPs with IR780, gambogic acid (HSP90 inhibitor), and MnO_2 co-delivery to achieve better antitumor efficacy with enhanced PDT and PTT via relieving hypoxic TME and restraining HSP90, respectively [21]. To achieve better antitumor efficacy by alleviating hypoxic TME and suppressing HSP90 to enhance PTT, respectively.

Recently, natural bioactive compounds have emerged as promising candidates to enhance the antitumor efficacy of chemotherapy, PDT, PTT, and immunotherapy [22,23]. GL, a naturally occurring triterpenoid glycoside derived from the Glycyrrhiza glabra (licorice), exhibits multifaceted anti-tumor properties, including inhibiting tumor cell proliferation, metastasis, angiogenesis, and activating the tumor immune suppression [24,25]. The previous studies have reported that GL efficiently facilitated anti-tumor immunity by attenuating Tregs and MDSCs, inhibiting the release of HMGB1, which would result in a persistent tumor immune-suppressive microenvironment, and regulating response to immune checkpoint blockade [26,27]. Owing to the selective binding capacity of GL to the specific receptors on HCC cells, GL-modified nanocarriers facilitated the enhanced HCC tumor accumulation and cell internalization [28,29]. In addition to the inherent anti-tumor benefits of GL, we have previously fabricated a GL-lipid framework nanosystem for triptolide delivery, to substitute cholesterol by means of the steroid structure of GL, with better HCC targeting and stability in comparison to conventional liposomes [30]. Analogously, we employed the GL-lipid NPs to load photosensitizer chlorin e6 (Ce6) for in situ psoriasis chemo-phototherapy, via the synergistic effects on modulating immune cell recruitment and inhibiting dendritic cell maturation [31].

Interestingly, our preliminary experiment suggests that GL may function as an efficient HSP90 inhibitor. Taking the immunomodulatory effects and specific drug delivery advantages of GL into consideration, we propose a proof-of-concept design to efficiently encapsulate IR780 with our fabricated GL-lipid NPs for HCC treatment. This combination system could embody the “all-in-one” merit to overcome the drawbacks of IR780-mediated phototherapy, including enhanced tumor-targeted delivery of IR780, mitigation of HSP90 overexpression, and reversal of the immunosuppressive tumor microenvironment (TME), thereby potentiating antitumor immune responses and therapeutic outcomes. This study is the first attempt to develop the application of GL-based lipid nanoparticles for the chemo-phototherapy against HCC. As illustrated in the Graphical abstract, the IR780 GLPs not only enhance the in vivo circulation time and tumor-targeting efficiency of IR780 but also serve as a functional carrier to suppress HSP90 expression, thereby augmenting the PTT efficacy. Furthermore, the immunomodulatory properties of GL contribute to the remodeling of the immunosuppressive tumor microenvironment, collectively facilitating a robust and sustained PTT-mediated antitumor immune response.

2. Materials and methods

2.1. Chemicals and reagents

Egg yolk phospholipids (EYPC) were obtained from A.V.T. Pharmaceutical Co., Ltd. (Shanghai, China). Cholesterol (CHO, purity ≥98 %) was provided by Aladdin Biochemical Technology Co., Ltd. (Shanghai, China). GL (purity ≥98 %) was obtained from Dalian Meilun Biotechnology Co., Ltd. (Dalian, China). IR-780 iodide was obtained from Macklin Co., Ltd. (Shanghai, China). The CCK-8 kit was obtained from Bioground Co., Ltd. (Chongqing, China). JC-1 kit and Annexin V-fluorescein isothiocyanate (FITC)/propidium iodide (PI) apoptosis kit was purchased from 4A Biotech Co., Ltd (Suzhou, China). The ELISA kits (IL-10, IL-12, TGF-β, IFN-γ, and TNF-α) were acquired from Boster Biological Technology Co., Ltd (Wuhan, China). Human hepatocarcinoma cell line (HepG2), mouse hepatocarcinoma cell line (H22) and telomerase-immortalized human liver epithelial cells-2 (THLE-2) were procured from the Chinese Academy of Medical Sciences Co., Ltd. (Shanghai, China). BALB/c nude mice (4 weeks old, 14–16 g) and male ICR mice (4 weeks old, 20–25 g) were purchased from SPF Biotechnology Co. Ltd. (Beijing, China). The animal-related experiments were conducted according to the Experimental Animals Administrative Committee of Chengdu University of Traditional Chinese Medicine (permission number: SYXK2020-124).

2.2. Preparation and characterization of IR780 GLPs

Based on previous research, GL-lipid hybrid NPs were fabricated using the solvent injection method. Briefly, GL (6 mg), EYPC (30 mg), and IR780 (1 mg) were dissolved in 2 mL of ethanol. The mixture was then dropwise added into 10 mL of Millipore water at 45 °C at a constant rate of 1 mL/min. The suspension was kept stirring at 45 °C for 2 h and was sonicated for 5 min in an ice bath with a cycle of 2 s of sonication followed by 3 s of rest. After we removed the residual ethanol in the NPs suspension by rotary evaporator, the unloaded free drugs in suspension were removed by ultracentrifugation at 19960×*g* for 40 min (Thermo Scientific, Sorvall ST4 centrifuge). The free drug would be placed in supernatant. The sediment was collected and resuspended with a small quantity of Millipore water to obtain the IR780 GLPs. The obtained IR780 GLPs suspension was stored at 4 °C for use. Similarly, GL in this formula was replaced with an equal amount of cholesterol to prepare the IR780-loaded liposomes (IR780 LPs) as the control of IR780 GLPs.

The particle size, zeta potential, and polydispersity index (PDI) of the IR780 GLPs were measured by a dynamic light scattering (DLS) instrument with a Malvern Zetasizer (Nano ZS90, Malvern Instruments, UK). The NPs morphological analysis was performed with a transmission electron microscope (TEM, JEOL JEM 1200EX, Japan). The storage stability of IR780 GLPs at 4 °C was evaluated by monitoring the particle size and PDI values continuously over one week. The drug encapsulation efficiency [11] and loading efficiency (LE) of IR780 and GL in IR780 GLPs were tested by high-performance liquid chromatography (HPLC) analysis. Briefly, 1 mL of the IR780 GLPs suspension was mixed with 3 mL of methanol and extracted via ultrasonication for 5 min. The suspension was filtered by a 0.22 μm filter before HPLC analysis. After filtration through a 0.22 μm filter, 10 μL of suspension was injected into HPLC and the mobile phase of HPLC analysis for IR780 and GL determination was 0.2 % formic acid-methanol/0.2 % formic acid water (85:15, v/v) and methanol/0.1 % phosphoric acid water (75:25, v/v), at measurement wavelengths of 780 nm and 250 nm, respectively.

2.3. Membrane structure characterization by small-angle and wide-angle X-ray scattering (SAXS/WAXS) analysis

The structural characterization of IR780 GLPs was performed using a Xeuss 2.0 system (Xenocs, France) equipped with a micro-focused Cu Kα X-ray source (λ = 0.15418 nm, 45 kV/0.6 mA) and a Pilatus 3R 300K 2D detector (pixel size: $172 \times 172\ \mu m^2$). The nanoparticle dispersion (2 mL) was loaded into a radiation-compatible quartz capillary (1.5 mm diameter) and analyzed under temperature-controlled conditions (25.0 ± 0.5 °C). SAXS data were collected at a sample-to-detector distance of 1188.0 ± 0.5 mm, while WAXS measurements employed a distance of

94.9 ± 0.1 mm. SAXS 2D patterns were processed using FIT2D v18.007 software, integrated over a $55^\circ < \varphi < 125^\circ$, and background-subtracted to generate the scattering intensity profile I(q). Guinier analysis was applied to the $\ln q < -1$, where lnI(q) versus q^2 yielded a linear fit for calculating the radius of gyration (Rg) via the Guinier equation ($\ln I(q) = \ln I(0) - q^2 Rg^2/3$). The hydrodynamic radius (R) was derived from the relation $R = \sqrt{\frac{5}{3}} Rg$ and SAXS data were further fitted using SasView 5.0.6 with a Core-Multishell model (fixed core radius is 57.8 ± 0.3 nm). Lipid bilayer thickness was calculated by fitting SAXS data with the scattering model $I(q) = \mathrm{cale}/V \cdot [3V(\Delta\rho)(\sin(qr) - qr\cos(qr))/((qr)^3)]^2 + \mathrm{background}$, generating probability distribution profiles, while WAXS 2D diffraction patterns were acquired and processed using FIT2D with geometric correction.

2.4. *Drug release in vitro*

2 mL of IR780 GLPs suspension was enclosed in a dialysis bag (MW cutoff, 3500) containing 30 mL of PBS (pH 7.4) with 1 % Tween 80, and dialysis at 37 °C and 120 rpm in an oscillating incubator. 1 mL samples were collected periodically, and an equal volume of fresh dialysis medium was added. Drug release rates were determined by HPLC, and cumulative release was calculated accordingly.

2.5. *Photothermal performance test*

A volume of 100 μL of each sample type (IR780 GLPs, Free IR780, Free GL, and ultrapure water) was placed in a 1.5 mL centrifuge tube, with the irradiation for 60 s at a wavelength of 808 nm at three different powers (0.6 W/1.7 A, 1.0 W/2.0 A, 2.2 W/3 A). The temperature variation of the samples was monitored at different time points. The temperature profiles of the IR780 GLPs were recorded utilizing a handheld thermal imaging camera (HTI HT-19, Xintai, China).

2.6. *Cellular uptake in vitro*

The internalization of IR780 GLPs by HepG2 cells was examined using flow cytometry and confocal microscopy. HepG2 cells were seeded in 24-well plates and incubated overnight. The medium was replaced with solutions of free IR780 (20 nM), free GL + IR780 and IR780 GLPs for 1, 2 and 4 h. Post-incubation, the cells were fixed, stained, washed, and imaged using confocal laser scanning microscopy (CLSM, FV10i, Olympus, Japan) to observe the intracellular distribution and uptake of IR780 GLPs. The uptake of IR780 GLPs in HepG2 cells was quantified by flow cytometry (FCM, FACS Calibur, BD Biosciences, USA).

2.7. *Cell cytotoxicity assay*

The cytotoxicity of IR780 GLPs towards HepG2 cells and THLE-2 cells was evaluated using the CCK-8 kit. HepG2 cells (6.0×10^4 cells/mL) were cultured in a 96-well plate and exposed to IR780 GLPs for 48 h. A range of concentrations of Free GL (0–130 μM), Free IR780 (0–32 μM), Free GL + IR780, Blank GLPs and IR780 GLPs were applied for 4 h coculture. Cells were irradiated with an 808 nm laser at 0.6 W/cm^2 for 3 min, and then cultured for 48 h at 37 °C sequentially. After that, cells were treated with CCK-8 solution, and the absorbance was measured at 450 nm using a microplate reader. The same operation was performed on THLE-2 cells.

2.8. *Mitochondrial membrane potential and Annexin V-FITC/PI double staining assay*

The cell apoptosis of HepG2 cells induced by IR780 GLPs was evaluated by the MMP and Annexin V-FITC/PI double staining assay. HepG2 cells were seeded into 12-well plates at a density of 2×10^5 cells/well and then incubated with fresh medium (0.5 % FBS) containing free GL + IR780, Blank GLPs, IR780 LPs, and IR780 GLPs for 4 h. The final concentrations of IR780 and GL were 2.48 μM and 10.19 μM, respectively. After that, the medium was replaced with fresh medium and irradiated with an infrared laser at a wavelength of 808 nm and 0.6 W/cm^2 for 3 min, followed by further incubation for 48 h. Subsequently, the fresh culture medium containing JC-1 dye was employed to replace the previous medium for 20 min incubation at 37 °C in a CO_2 incubator. The cells were washed twice with cold PBS and examined by FCM. The ratio of red/green fluorescence was calculated for the quantitative assessment of mitochondrial polarization states.

Similarly, after overnight culture, HepG2 cells (2.0×10^5 cells/mL) were incubated with the same treatments for 4 h, followed by 3 min of laser irradiation (808 nm, 0.6 W/cm^2). The cells were then incubated for an additional 48 h, collected and stained with Annexin V-FITC/PI (1.0 mg/mL), and the apoptosis rate was determined via flow cytometry. The data were analyzed using the software FlowJo (BD Biosciences, USA).

2.9. *Macrophage polarization assays*

RAW 264.7 macrophages were seeded in 12-well plates at a density of 2.0×10^5 cells/well for 24 h and then incubated with IL-4 (20 ng/mL) + IL-13 (20 ng/mL) for 24 h to induce the M2-type macrophage. Cells were treated for 4 h with free GL + IR780, Blank GLPs, IR780 LPs, and IR780 GLPs containing equal amounts of IR780 and GL (2.48 μM and 10.19 μM). Following this, cells were exposed to laser irradiation (808 nm, 0.6 W/cm^2) for 3 min. After 24 h of incubation and staining with anti-CD86 and anti-CD206 antibodies, expression levels of the index were measured by FCM.

2.10. *Distribution of IR780 GLPs in vivo*

To assess the distribution of IR780 GLPs in vivo, tumor-bearing mice were randomly assigned and intravenously administered with free IR780, free GL + IR780, IR780 LPs, or IR780 GLPs (with an equal IR780 dosage of 2 mg/kg). The IVIS Lumina Series imaging system captured images at 2, 5, 8, 12, 24, 36, 48, and 60 h post-injection. Subsequently, mice were anesthetized and euthanized after a 60-h observation period, and their tumors and major organs, including the heart, lungs, liver, spleen, and kidneys, were harvested for *ex vivo* imaging.

2.11. *Molecular docking analysis and molecular dynamics simulation*

The HSP90α structure was predicted via AlphaFold3, optimized with Rosetta relaxation, and preprocessed (dehydration/hydrogenation) in PyMOL. The GL structure was retrieved from PubChem(https://pubchem.ncbi.nlm.nih.gov/). Blind docking was performed via the CB-DOCK2 web server, which executes AutoDock Vina for ligand-receptor docking and 3D visualization in PyMOL.

Molecular docking between GL and HSP90 was performed, and the resulting complexes were subjected to all-atom molecular dynamics (MD) simulations using GROMACS 2023.3 for 100 ns. Energy minimization was conducted using the steepest descent method under the NVT ensemble, followed by 100 ps NVT and NPT equilibrations to stabilize temperature and pressure. The LINCS algorithm was used to constrain hydrogen bonds with a 2 fs integration step. Electrostatic interactions were calculated by the Particle Mesh Ewald (PME) method with a 1.2 nm cutoff, and non-bonded interactions was updated every 10 steps. After simulations, trajectories were processed for periodicity removal and analyzed for RMSD, RMSF, radius of gyration (Rg), and hydrogen bond numbers.

2.12. *In vivo Anti-HCC Affect*

An HCC tumor-bearing mouse model was constructed by subcutaneously injecting H22 cells in 100 μL 50 % Matrigel-containing PBS into the right axilla of ICR mice. When the tumor volume reached approximately 100 mm^3, tumor-bearing mice were injected every other day via the tail vein with saline, Blank GLPs, free GL + IR780, IR780 LPs, or IR780 GLPs, all containing equal concentrations of GL (2.8 mg/kg) and IR780 (0.6 mg/kg). After 24 h post-injection, the mice in the irradiation groups were subjected to an 808 nm laser irradiation at 0.6 W/cm^2 for 3 min for the first three doses. The temperature changes at the tumor site were continuously monitored. A handheld infrared thermal imaging camera (HTI HT-19, Xintai, China) was used to record the temperature distribution at different time points during irradiation. Tumor volume and body weight were monitored every other day over a 14-day period. At the end of the study, the mice were anesthetized with pentobarbital sodium and blood samples were collected. Tumors and major organs (heart, lungs, kidneys, liver, and spleen) were excised, and tumor dimensions were photographed and weighed. Additionally, HSP90 expression was analyzed by Western blotting (WB) using tumor tissue, and HSP90 staining in tumor tissues was performed using immunofluorescence staining with a specific anti-HSP90 antibody.

The tumor tissue sections were prepared using the paraffin embedding method. Hematoxylin and eosin (H&E) and immunohistochemistry (IHC) for matrix metalloproteinase-9 (MMP-9), E-cadherin (E-cad) and cluster of differentiation 31 (CD31) staining was performed. Furthermore, serum levels of interleukin-10 (IL-10), transforming growth factor-beta (TGF-β), tumor necrosis factor-alpha (TNF-α), interferon-gamma (IFN-γ), and interleukin-12 (IL-12) were measured using enzyme-linked immunosorbent assay (ELISA) kits to evaluate immune modulation, the optical density (OD) values were measured with a microplate reader and the respective concentrations were calculated according to the standard. In addition, tumor tissues were dissociated into single-cell suspensions, stained with antibodies against mouse CD3, CD4, CD8, CD45 (T cell markers) and antibodies specific for CD206, CD86, F4/80 (macrophage markers), and analyzed by flow cytometry to assess immune cell populations. Organs (heart, liver, spleen, lung, kidney) were processed for H&E staining to assess potential organ toxicity or damage induced by IR780 GLPs.

2.13. Statistical analysis

All data are presented as means ± standard deviation from three independent experiments. Statistical differences were evaluated using one-way ANOVA, with values of $p < 0.05$, 0.01, and 0.001 considered statistically significant and labeled as *, **and ***, respectively). NS indicated no significance.

3. Results and discussion

3.1. Preparation and characterization of IR780 GLPs

Building upon previous research, GL/IR780 nanoparticles were successfully synthesized via the ethanol injection method (Fig. 1A–a). GL possesses amphiphilic properties, with hydrophobic triterpenoid structures and hydrophilic glucuronic acid residues. During liposome formation, the hydrophobic moiety of GL inserts into the lipid bilayer by interacting with the hydrophobic acyl chains of phospholipids, while the hydrophilic groups of GL orient toward the aqueous environment, stabilizing the liposomal membrane and partially substituting for the role of cholesterol. Furthermore, the WAXS 2D diffraction pattern (Fig. 1A–b) exhibited a circularly symmetric intensity distribution, confirming the isotropic spherical morphology of GL liposomes. Guinier analysis of SAXS data (Fig. 1A–c) yielded a radius of gyration of 44.73 nm, corresponding to a radius R of 57.80 nm. Core-Multishell model fitting (Fig. 1A–d) quantitatively resolved the lipid bilayer thickness as 28.21 nm. In addition, their morphology and particle distribution are presented in Fig. 1B and C. DLS measurements showed that the IR780 GLPs had an average particle size of 120 ± 2.8 nm and a PDI of 0.16 ± 0.02, indicating good dispersion uniformity. TEM imaging confirmed that the nanoparticles exhibited a well-defined spherical morphology with smooth surfaces and a uniform size distribution. The zeta potential was measured at −24.2 ± 1.88 mV, confirming the negative charge and stability of the particles, consistent with the TEM findings. HPLC analysis revealed an encapsulation efficiency of 92.88 ± 0.33 % and a drug loading capacity of 15.07 ± 0.28 % for GL, while IR780 exhibited an encapsulation efficiency of 97.34 ± 0.24 % and a drug loading capacity of 1.93 ± 0.12 %. After storage at 4 °C for seven days (Fig. 1D), the particle size remained stable within the range of 105–112 nm, and the zeta potential ranged from −18 to −24 mV. The nanoparticle suspension remained clear and free of precipitation, demonstrating excellent formulation stability.

The dialysis method was used to simulate the in vivo drug release behavior of IR780 and GL from IR780 GLPs. The IR780 GLPs were immersed in PBS (0.1 % Tween 80, pH 7.4) over 12 h. As shown in Fig. 1E, free IR780 exhibited rapid release, achieving 88 % cumulative release within 8 h, whereas the IR780 encapsulated in IR780 GLPs demonstrated sustained release with only 37 % cumulative release during the same period. Similarly, free GL displayed rapid release behavior, with a cumulative release of 91 % cumulative release at 8 h (Fig. 1F), in stark contrast to the slow release from IR780 GLPs, which released 32 % of GL over 12 h. These results demonstrate that IR780 GLPs encapsulation significantly delays drug release compared to free drug formulations, highlighting the sustained-release characteristics of the nanoparticle system.

The photothermal performance of IR780 GLPs was evaluated under three NIR laser power densities with real-time temperature monitoring. As shown in Fig. 1G, the temperature increase at 0.6 W/1.7 A was slower compared to 1.0 W/2.0 A and 2.2 W/3.0 A. Based on this observation, subsequent photothermal performance evaluations were conducted using 0.6 W/1.7 A. As illustrated in Fig. 1H, water and the free GL exhibited non-significant temperature changes under infrared laser irradiation. The free IR780 group, containing the same amount of IR780, showed a rapid temperature increase to 52 °C within 60 s. In contrast, IR780 GLPs exhibited a more gradual temperature rise, reaching 44.6 °C in 60 s. Similarly, Infrared thermography visually demonstrated that the temperature of IR780 GLPs under near-infrared irradiation was lower than that of Free IR780 (Fig. 1I). These results suggest that after encapsulating in GLPs, IR780 attenuates milder PTT capacity under 0.6 W/1.7 A laser irradiation, compared to the free IR780, which would show better biosafety.

3.2. Cellular uptake of IR780 GLPs

The enhanced cytotoxicity of nanoparticles toward cancer cells can be attributed to their improved cellular internalization [32]. As illustrated in Fig. 2A, free IR780 exhibited weak red fluorescence in HepG2 cells, indicating limited uptake, whereas IR780 LPs displayed significantly stronger fluorescence signals. Notably, IR780 GLPs exhibited even higher fluorescence intensity than IR780 LPs, suggesting glycyrrhizin-mediated targeting enhances hepatocellular carcinoma-specific uptake. Furthermore, quantitative uptake analysis (Fig. 2B and C) confirmed that the fluorescence intensity of the nanoparticle formulations was consistently higher than that of the free IR780 groups. Additionally, as the incubation time increased from 1 h to 4 h, fluorescence intensity correspondingly increased, demonstrating the time-dependent uptake of IR780 GLPs by HepG2 cells.

3.3. Cytotoxicity of IR780 GLPs

As shown in Fig. 2D, free GL demonstrated minimal inhibitory effects on HepG2 cell proliferation, with blank GLPs showing only 20 % inhibition at 128 μM, consistent with prior findings[27]. In contrast, free IR780 and free IR780+GL combination exhibited enhanced cytotoxicity under photothermal conditions, reducing cell viability to 45–55 % at 32 μM, with no significant interference from GL on cytotoxic effect of IR780. Notably, IR780 GLPs displayed superior antiproliferative effects

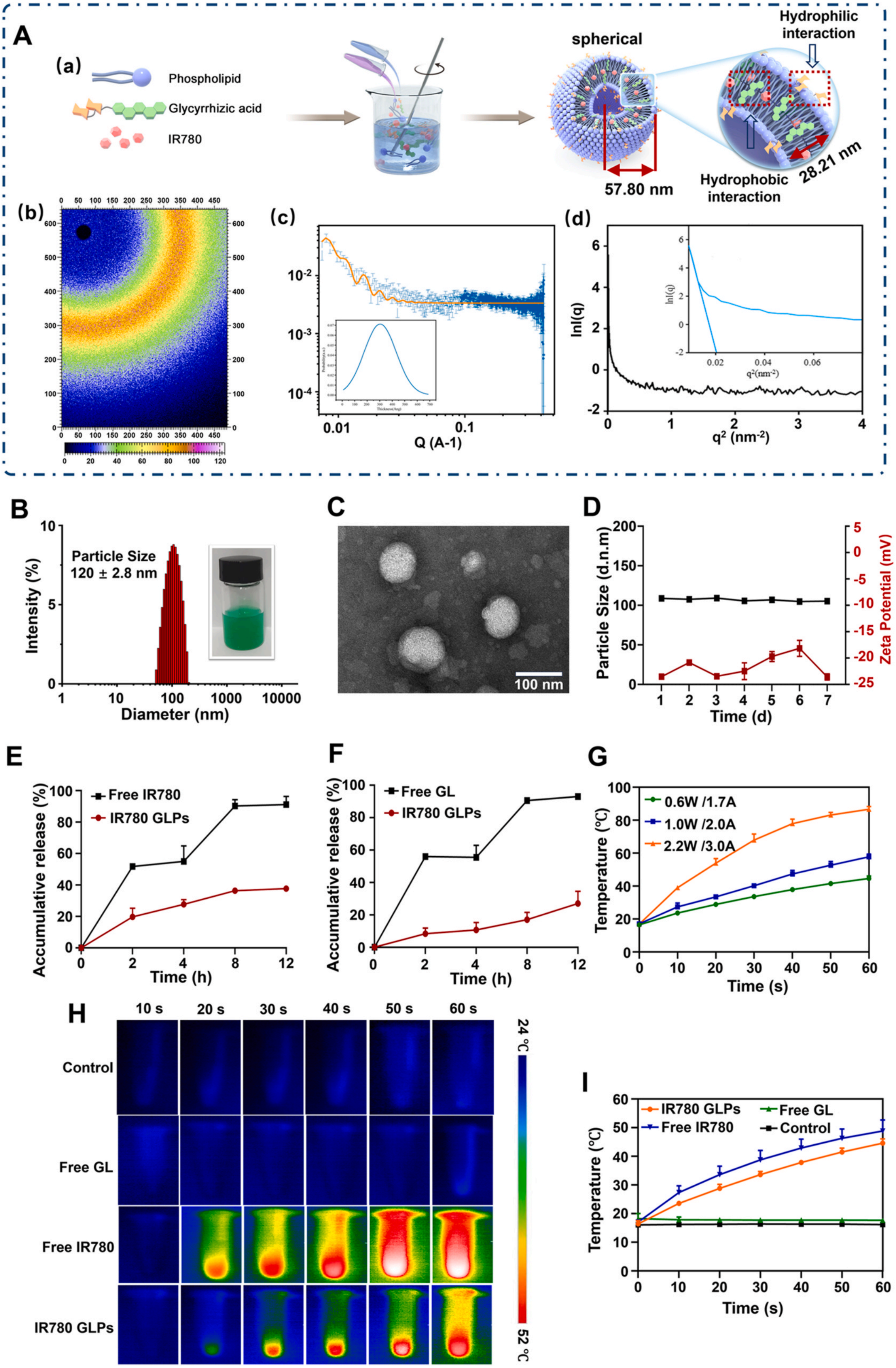

Fig. 1. Characterization of IR780 GLPs. (A) The preparation process of IR780 GLPs and morphological analysis. (a) Preparation process, (b) Wide-angle scattering two-dimensional diagram. (c) SAXS data analysis, (d) The Guinier plot analysis. (B) DLS particle size distribution and representative photos of IR780 GLPs. (C) TEM morphology of IR780 GLPs. (D) Storage stability at 4 °C for 7 d. Drug release profiles of IR780(E) and GL(F) from IR780 GLPs in vitro. (G) Temperature change curve of IR780 GLPs solution under different power irradiation. (H) Thermal images of IR780 GLPs at various concentrations under NIR laser irradiation (0.6 W/1.7 A) and (I) corresponding photothermal curves.

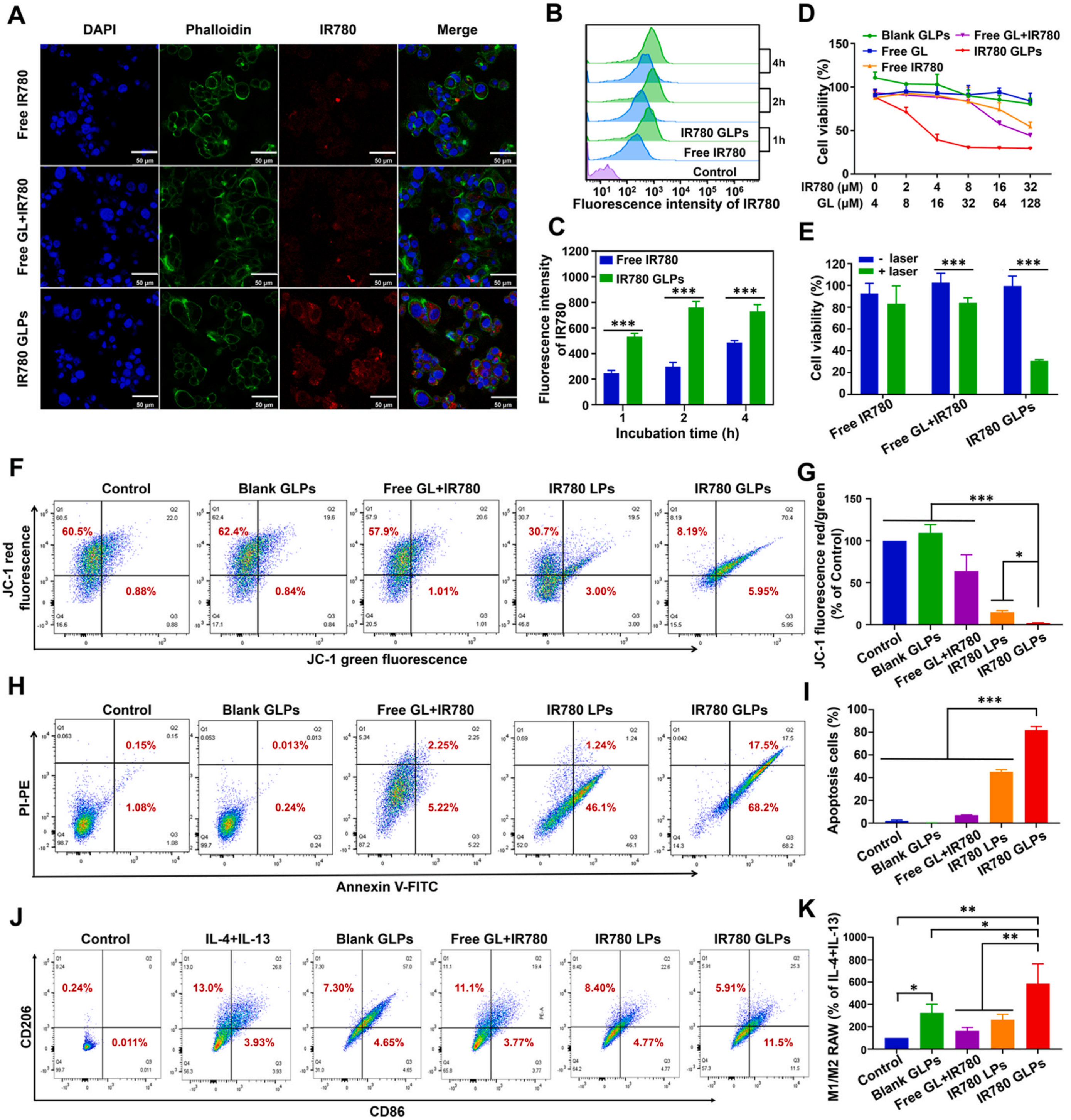

Fig. 2. Cellular uptake, cytotoxicity, apoptosis and M1/M2 macrophage polarization of IR780 GLPs in vitro. (A) CLSM images of the cellular internalization. Scale bar = 50 μm. (B) Flow cytometric histogram profiles of the fluorescence intensities in each treatment group and (C) mean fluorescence value of each group. (D) Cytotoxicity of IR780 GLPs against HepG2 cells with laser irradiation and (E) comparison of cytotoxicity between different groups with or without laser irradiation. (F) FCM investigation of MMP alterations in different treatment groups, and (G) quantitative analysis. (H) FCM detection of apoptosis following different treatment groups with Annexin V-FITC and PI staining and (I) quantitative analysis. (J) Expression of mean positive cells of $CD206^+$ and $CD86^+$ determined by FCM and (K) Quantitative analysis.

compared to Free IR780, achieving 70 % inhibition at 8 μM and an IC50 value of 2.48 μM, suggesting enhanced cytotoxicity attributed to improved cellular internalization.

Additionally, cellular viability was evaluated both with and without NIR laser irradiation (Fig. 2E). In the absence of irradiation, all treatment groups exhibited minimal inhibition. Upon exposure to NIR laser irradiation, however, significant inhibition was observed across all groups, with IR780 GLPs exhibiting the most pronounced suppression. These findings indicate that IR780 GLPs possess favorable biocompatibility and can efficiently exert cytotoxic effects upon NIR laser activation. Furthermore, the cytotoxicity of IR780 GLP towards normal human liver cells was assessed using the THLE-2 cell line. As shown in

Supplementary Fig. S1, IR780 GLP exhibited no significant cytotoxicity across the tested concentration range, with cell viability consistently exceeding 80 % in all treatment groups.

3.4. *IR780 GLPs enhanced the HepG2 cell apoptosis*

MMP loss, a hallmark of early apoptosis, was assessed in HepG2 cells via JC-1 fluorescence staining [33]. Intact MMP promotes JC-1 aggregation (red fluorescence), while depolarization shifts emission to JC-1 monomers (green). As shown in Fig. 2F and G, blank GLPs caused no significant MMP disruption compared to untreated controls, aligning with the negligible cytotoxicity of GL. Strikingly, however, compared to IR780 LPs, the IR780 GLPs group showed a significantly lower JC-1 green/red fluorescence ratio. This indicates that GL-functionalized nanoparticles synergistically enhance IR780-mediated mitochondrial apoptosis initiation.

Apoptosis levels in HepG2 cells, a critical determinant of antitumor efficacy, were quantified via flow cytometry with Annexin V-PI dual staining. As shown in Fig. 2H and I, the blank GLPs group exhibited negligible apoptosis at a GL concentration of 10.19 μM, indicating that GL exerted minimal cytotoxicity on HepG2 cells at this concentration. However, compared to the Free GL + IR780 group, the IR780 LPs group showed a significant increase in apoptosis, with a total apoptosis rate of 47.34 %. Notably, the IR780 GLPs group demonstrated the most pronounced effect, with a total apoptosis rate of 85.7 %, including an early apoptosis rate of 68.2 % and a late apoptosis rate of 17.5 %. Collectively, these findings demonstrate that IR780 GLPs achieve synergistic antitumor efficacy through GL-directed tumor targeting and photothermal activation.

3.5. *Tumor-associated macrophage (TAM) polarization of IR780 GLPs*

In the tumor microenvironment (TME), macrophages are one of the most abundant immune cell populations. Their polarization between the pro-inflammatory, antitumor M1 phenotype and the immunosuppressive, tumor-promoting M2 state plays a crucial role in tumor progression and development. Therefore, activating relevant pathways to repolarize M2 macrophages into the M1 phenotype has become a common strategy to enhance the efficacy of immunotherapy [34].

Macrophage polarization was induced using IL-4 and IL-13 to establish an M2-dominant phenotype. As shown in Fig. 2J and K, the IL-4+IL-13 group exhibited a significantly higher M2 macrophage proportion compared to control group, confirming successful polarization. Following treatment with different groups, all groups showed reduced M2 proportions, with the IR780 GLPs group showing the most significant reduction to 5.91 %, accompanied by an increase in M1 macrophages to 11.5 %. Additionally, the M1/M2 ratio in the IR780 GLPs group was 5.8-fold higher than that of the IL-4+IL-13 group, 2.2-fold higher than that of the IR780 LPs group, and 3.3-fold higher than that of the GLPs group. These results indicate that GL effectively modulates macrophage polarization, promoting the transition of M2 macrophages into the antitumor M1 phenotype.

3.6. *In vivo biodistribution of IR780 GLPs*

The tumor targeting ability of IR780 GLPs in vivo was further evaluated using IVIS. Due to the intrinsic fluorescence properties of IR780, Free IR780, Free GL + IR780, IR780 LPs, and IR780 GLPs were intravenously injected into H22 tumor-bearing mice to assess their targeting efficiency. As shown in Fig. 3A and B, Free IR780 exhibited rapid metabolism, while IR780 GLPs demonstrated prolonged retention with strong tumor fluorescence signal persisting for 60 h, indicative of enhanced permeability and retention (EPR)-mediated tumor accumulation. Notably, the fluorescence intensity in the tumor site was significantly higher in the IR780 GLPs group than in the IR780 LPs group (Fig. 3C and D), which may be attributed to the active targeting capability of GL towards hepatocellular carcinoma cells, consistent with enhanced cellular uptake observed in HepG2 cells.

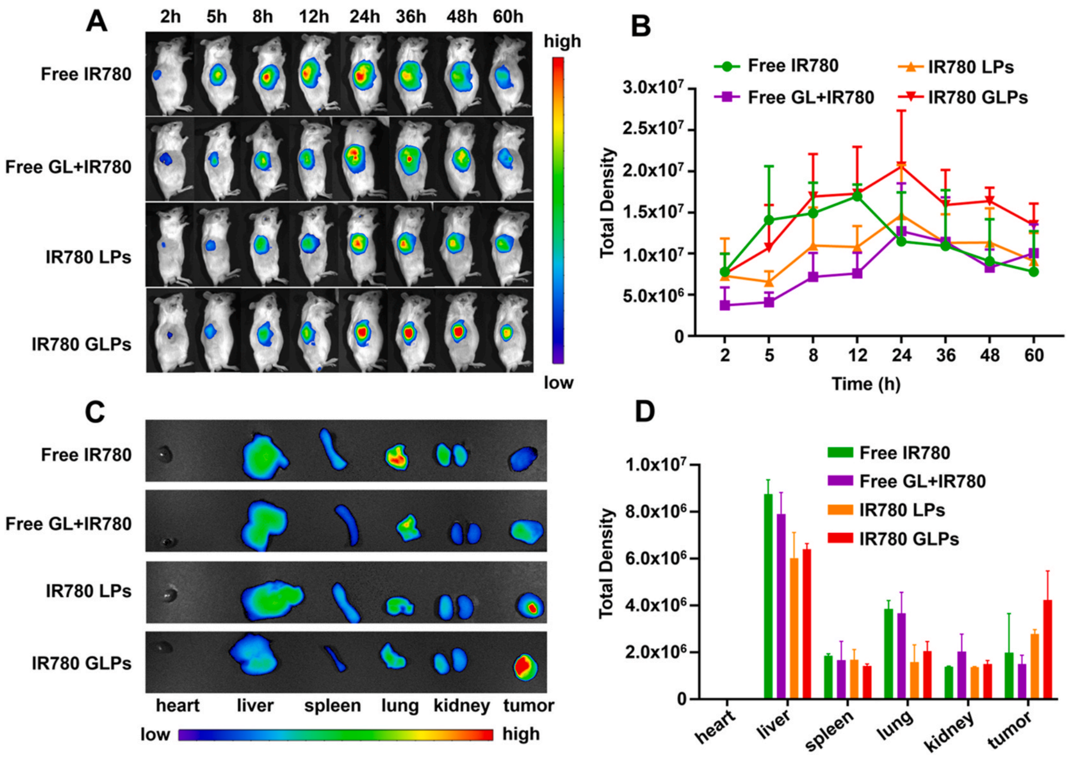

Fig. 3. In vivo distribution of IR780 GLPs. (A) In vivo real-time NIR fluorescence imaging and (B) fluorescence intensity statistics of H22 tumor-bearing mice after intravenous injection of various formulations. (C) Ex vivo images of tumors and organs at 60 h post-injection and (D) fluorescence intensity statistics.

3.7. In vivo antitumor efficacy of IR780 GLPs

The synergistic antitumor efficacy of IR780 GLPs was evaluated in H22 subcutaneous tumor-bearing mice (Fig. 4A). During laser irradiation, the temperature changes at the tumor site were monitored using an infrared thermal imaging camera. As shown in Fig. 4B and D, the tumor temperature in the IR780 GLPs group steadily increased and reached approximately 45 °C within 300 s, indicating effective photothermal conversion. In addition, tumor volume (Fig. 4E) and body weight (Fig. 4F) were monitored every two days over a 14-day treatment period. All treatment groups exhibited antitumor activity compared to controls, with IR780 GLPs showing the most pronounced effect. The average tumor volumes of the Free GL + IR780, blank GLPs, IR780 LPs, and IR780 GLPs groups were 44.74 %, 62.37 %, 32.02 %, and 15.29 % of the control group, respectively ($P < 0.05$). The tumor weight, as shown in Fig. 4G, was consistent with the tumor volume measurements on day 14. This result was also confirmed by the tumor tissue images (Fig. 4C). Critically, there was no significant change in body weight among any treatment group compared to the control group, indicating that the treatment is safe and does not induce severe side effects.

Furthermore, H&E-stained tumor sections (Fig. 5A) revealed that in the control group, tumor cells were densely arranged with clearly defined nuclei stained in deep blue, indicative of active tumor proliferation. In contrast, the IR780 GLPs group exhibited significant antitumor effects, characterized by evident nuclear shrinkage, sparse cell arrangement, and vacuole-like structures, suggesting tumor cell apoptosis.

IHC staining revealed the multifaceted antitumor mechanisms of IR780 GLPs (Fig. 5A–D). CD31, a well-established endothelial cell marker, is commonly used to assess tumor angiogenesis [35]. CD31-positive staining is indicated by brown punctate signals (red arrows). Notably, the IR780 GLPs group exhibited a significantly lower density of CD31 positive staining compared to the other groups, suggesting a potent inhibitory effect on tumor angiogenesis. Furthermore, E-cadherin expression, a metastasis suppressor, serves as an indicator of tumor metastatic potential [36]. We found that IR780 GLPs treatment significantly upregulated E-cadherin expression compared to other treatments, indicating enhanced cell adhesion and a reduced tumor metastasis. Concurrently, IR780 GLPs treatment resulted in a substantial reduction in MMP-9 expression, effectively mitigating extracellular matrix degradation and inhibiting tumor cell invasion.

3.8. The interaction between GL and HSP90

Molecular docking revealed stable interactions between GL and HSP90, with a predicted binding energy of −9.7 kcal/mol calculated by AutoDock Vina using the AMBER force field. PLIP server analysis of the protein-ligand complex, visualized via PyMOL, showed representative three-dimensional interactions as depicted in Fig. 6A, where GL formed hydrogen bonds (red) and salt bridges (yellow) with specific HSP90 residues, with bond lengths indicated beside dashed interaction lines. The ligand was positioned within the protein's binding cavity with low free energy, forming multiple non-covalent interactions, indicating the formation of a stable complex suitable for subsequent molecular dynamics simulations to assess binding stability.

Molecular dynamics simulation analyses were performed for a duration of 100 ns on GL and HSP90, utilizing the docking outcomes. The purpose was to assess the movement, path, structural attributes,

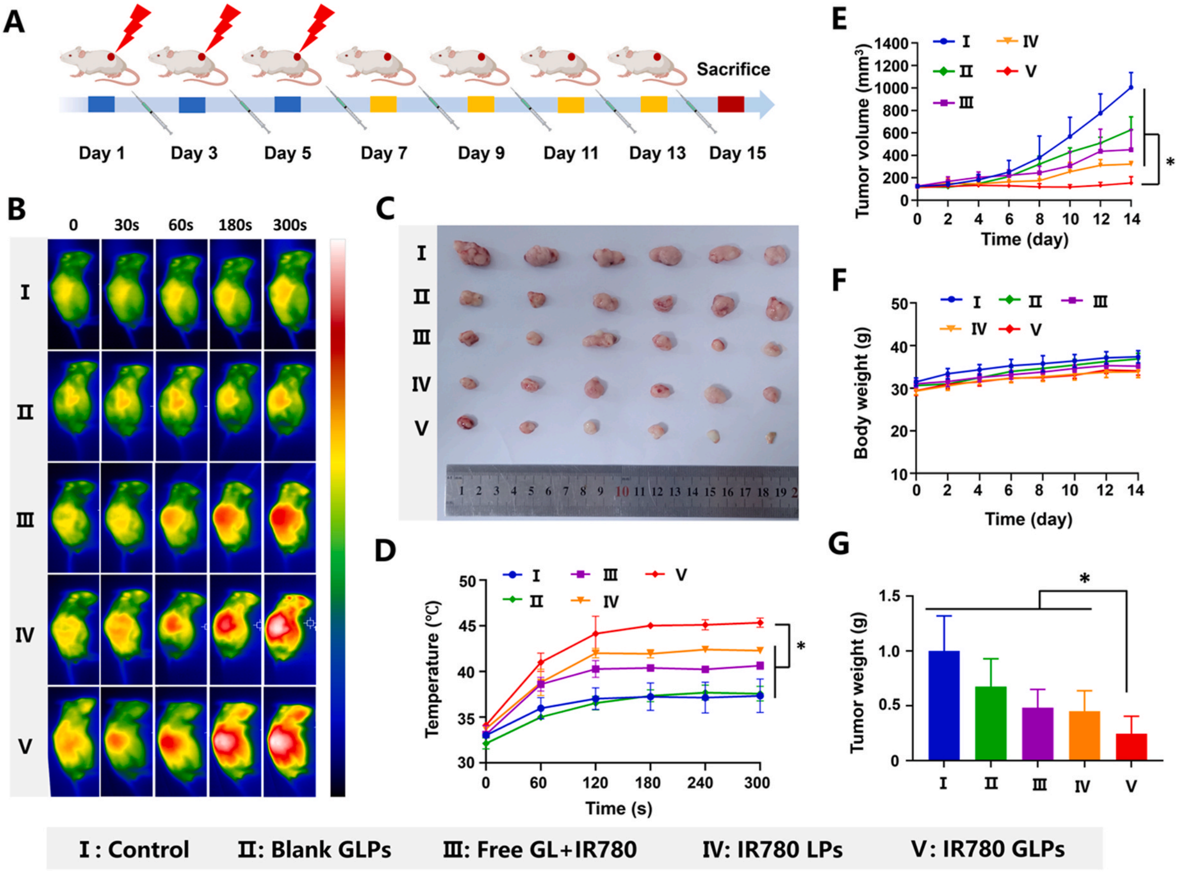

Fig. 4. Antitumor efficacy of IR780 GLPs in H22 tumor-bearing mice model. (A) Schematic illustration of the experimental regimen. (B) Thermal images of H22 tumor-bearing mice under near-infrared laser irradiation at different time points (0.6 W/1.7 A). (C) Representative photographs of tumors excised from each treatment group on day 15. (D) Corresponding photothermal curves. (E) Average tumor growth curves of different groups throughout the entire experiment period. (F) Body weight change curves. (G) Tumor tissue weight in each group of mice at the end of treatment. (Data are mean ± SD, n = 6, $^{*}P < 0.05$).

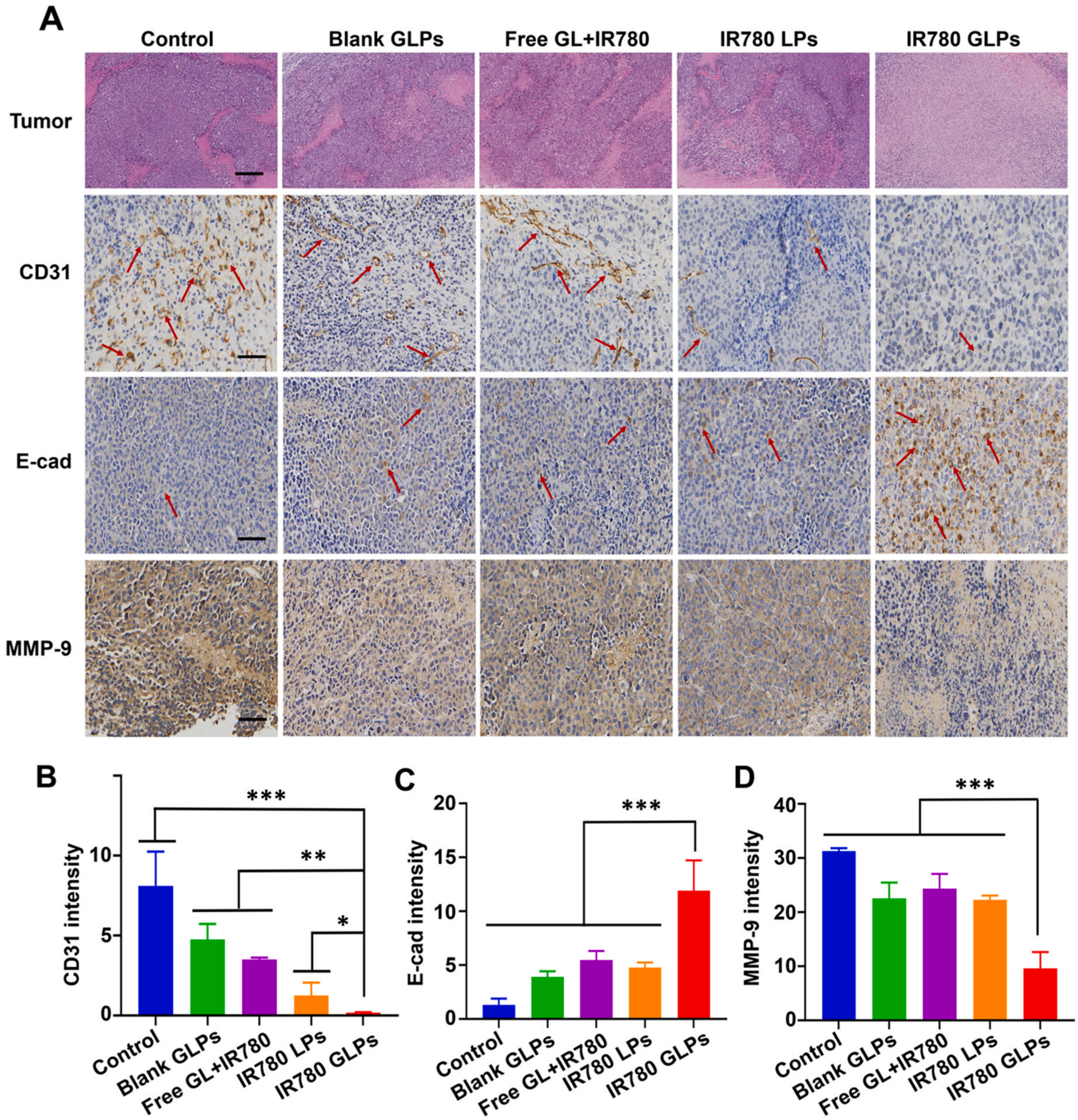

Fig. 5. In vivo antitumor effects of IR780 GLPs by immunohistochemical analysis. (A) H&E staining and IHC staining of CD31, E-cadherin, and MMP-9 in tumor tissues. The scale bar is 20 μm. Semiquantitative analysis for the positive percentage of CD31(B), E-cad(C), and MMP-9 (D) expression.

binding capacity, and alterations in conformation of these molecules. The RMSF analysis was conducted to assess the flexibility of each amino acid residue during the simulation. As shown in Fig. 6B, the overall RMSF values of the protein remained relatively low, indicating good structural stability. However, higher fluctuations were observed at the N- and C-terminal regions, which are less constrained by other protein domains. The increased RMSF in other regions may be attributed to ligand binding-induced perturbations or inherent flexibility of specific peptide segments. These findings suggest that the protein maintained stable dynamics during the simulation, with low structural perturbation. The RMSD analysis was performed to assess the stability and conformational changes of the ligand-protein complex during the simulation. As shown in Fig. 6C, it revealed that the complex exhibited slight fluctuations within the first 40 ns, then gradually stabilized around 0.4–0.5 nm for the remainder of the 100 ns. These results indicate that the ligand remained stably bound within the binding pocket without significant displacement, suggesting the formation of a stable and equilibrated complex. In addition, the number of hydrogen bonds between the small molecule and protein remained relatively stable throughout the simulation, fluctuating between 1 and 4 bonds, indicating stable binding (Fig. 6D). The radius of gyration (Rg) remained stable throughout the simulation, fluctuating around 4.0 nm, indicating minimal structural changes (Fig. 6E). MM/GBSA analysis (Fig. 6F) of the 90–100ns trajectory revealed that the binding energy between the small molecule and protein is dominated by van der Waals interactions (−73.76 kcal/mol), with electrostatic energy contributing −5.99 kcal/mol. Furthermore, it was noted that the solvation energy in this simulation was 3.21 kcal/mol, suggesting that the addition of the solvent was slightly unfavorable for the binding between small molecules and proteins. The overall binding free energy is −76.53 kcal/mol, suggesting a strong binding affinity. The dominant van der Waals interactions, along with hydrogen bonding and hydrophobic interactions, contribute to the stability of the protein-ligand complex.

Under PTT therapy, hyperthermia induces a heat shock response, leading to increased HSP90 expression, which in turn enhances tumor cell survival and reduces PTT efficacy [37]. Therefore, downregulation

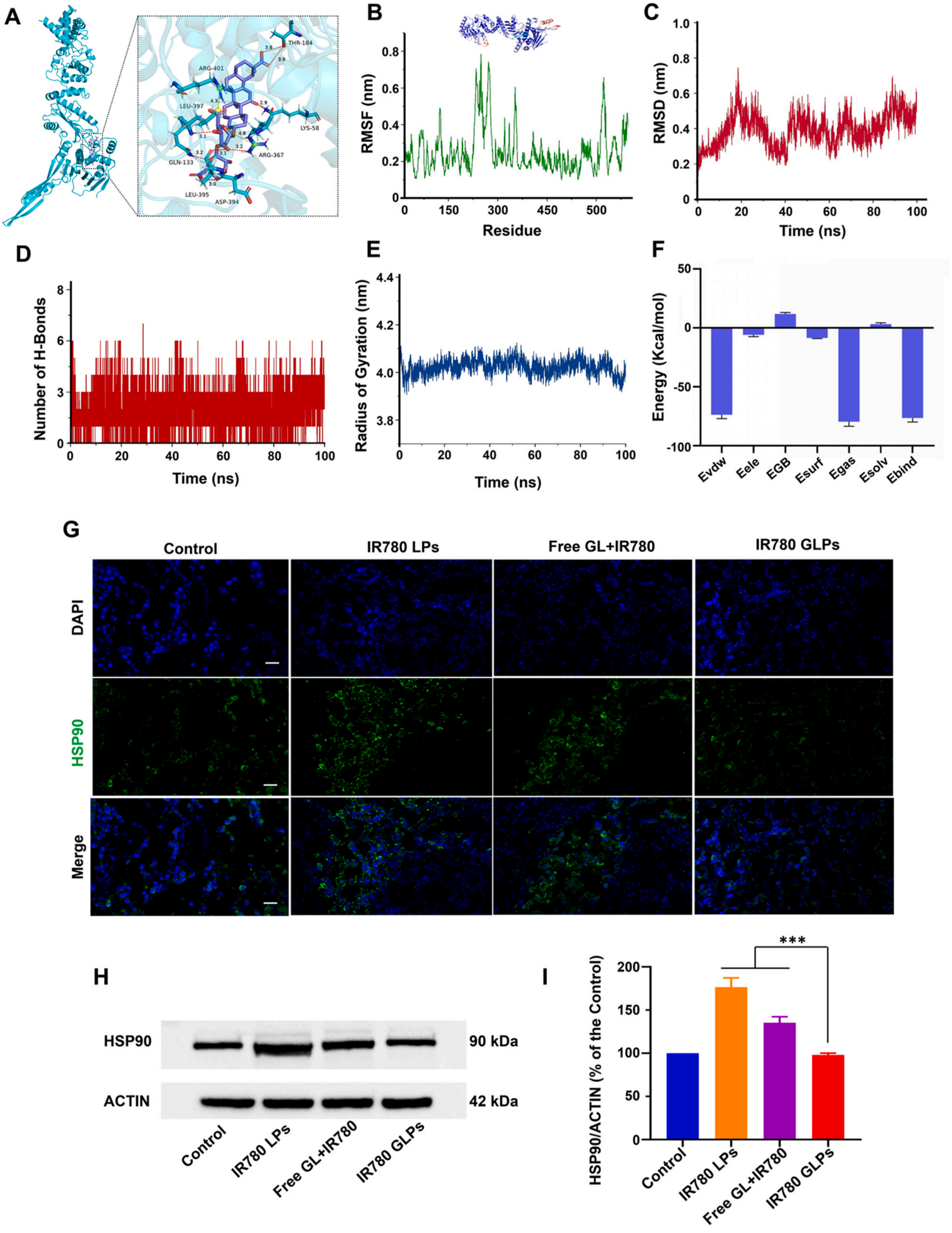

Fig. 6. Effects of IR780 GLPs on HSP90. (A) Receptor-ligand interactions between GL and HSP90. (B) RMSF distribution of amino acids in GL-HSP90. (C) Changes of RMSD values of GL-HSP90. (D) The number of hydrogen bonds between small molecules and proteins in GL-HSP90. (E) Changes of protein Rg values in GL-HSP90. (F) MM/GBSA analysis of GL and HSP90. (G) HSP90 immunofluorescence assessments in tumor tissue, with a scale bar of 20 μm. (H) Evaluation of HSP90 expression levels by Western blot analysis and (I) semiquantitative analysis of the HSP90 expression level.

of HSP90 represents a promising strategy to mitigate thermoresistance, enhance tumor cell apoptosis, and improve the overall therapeutic outcome of PTT. To investigate the regulatory effect of IR780 GLPs on HSP90 expression, tumor tissues were analyzed using HSP90 fluorescence staining and WB assays. As shown in Fig. 6G, following laser irradiation, the IR780 LPs and Free GL + IR780 groups exhibited HSP90 expression (indicated by green fluorescence), whereas no significant changes were observed in the IR780 GLPs group. This result suggests that GL effectively suppresses the mild PTT-induced upregulation of HSP90. Furthermore, as illustrated in Fig. 6H and I, the HSP90 expression level in the IR780 GLPs group comparable to that of the control group. These findings indicate that IR780 GLPs enhance tumor cell apoptosis under mild PTT by reducing HSP90 expression, thereby overcoming heat shock resistance and improving therapeutic efficacy.

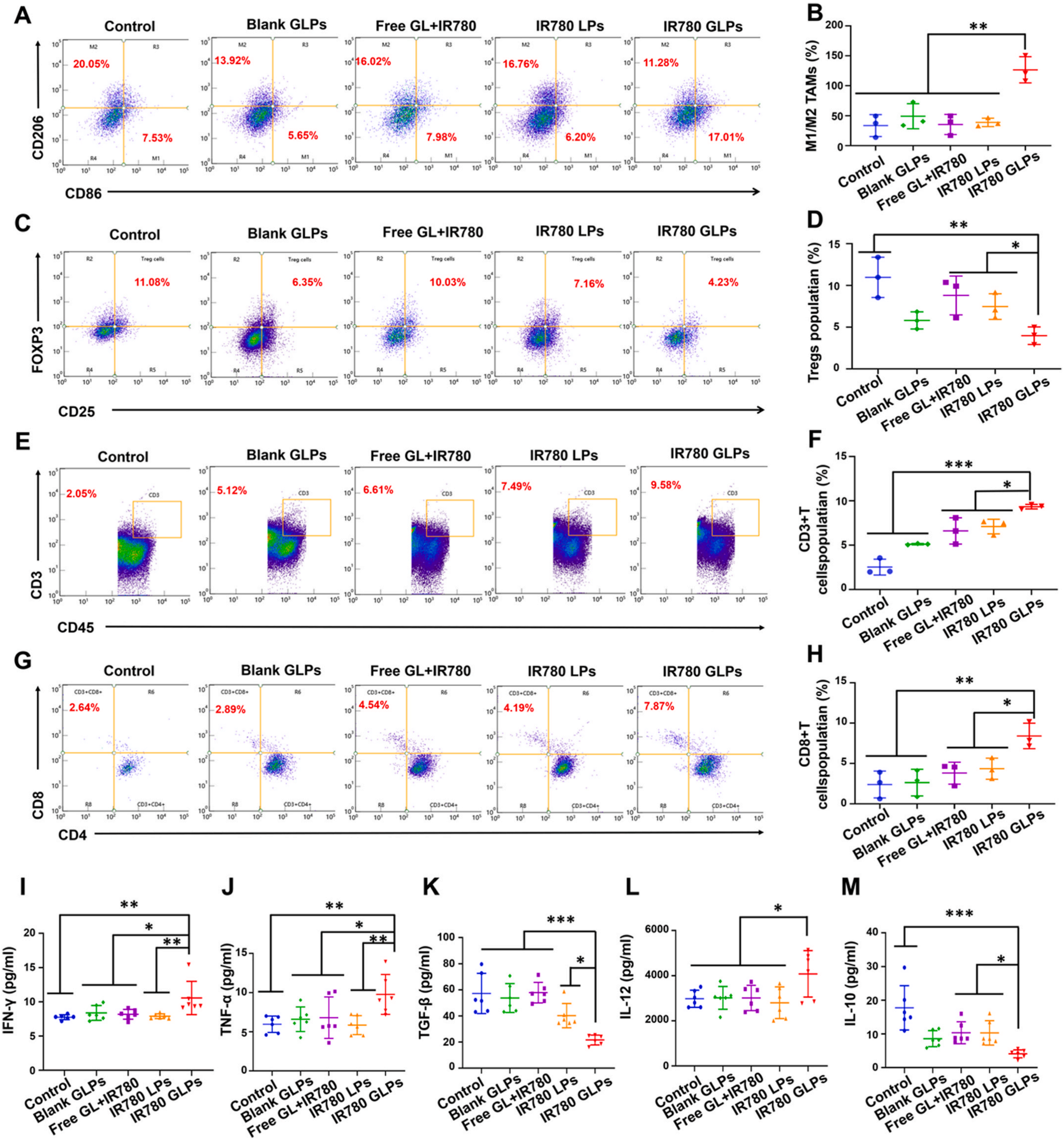

Fig. 7. In vivo antitumor immune mechanisms of IR780 GLPs. (A) Expression of mean positive cells of $CD206^+$ and $CD86^+$, determined by FCM and (B) Quantitative analysis of each group. (C) The positive rate of Treg cells expression detected by FCM and (D) statistical analysis of the proportion in each group. (E) Expression of mean positive cells for $CD3^+$ and $CD45^+$ and (G) $CD8^+$ and $CD4^+$, determined by FCM and (F) and (H) providing the quantitative analysis in each group. (I)Serum levels of IFN-γ, (J) TNF-α, (K) TGF-β, (L) IL-12, and (M) IL-10 detected by ELISA.

3.9. TME regulation effect of IR780 GLPs

Macrophage polarization plays a crucial role in tumor progression and immune modulation. As shown in Fig. 7A and B, compared to the control group, all treatment groups exhibited a reduction in M2 macrophage populations, with the IR780 GLPs group showing the most significant decrease. Concurrently, the proportion of M1 macrophages was markedly increased. The M1/M2 ratio in the IR780 GLPs group was 3.73-fold higher than that in the control group and 3.25-fold higher than that in the IR780 LPs group. However, no significant difference was observed between the control and IR780 LPs groups. These results suggest that IR780 GLPs effectively reprogram M2 macrophages into the M1 phenotype, thereby alleviating the immunosuppressive tumor microenvironment and potentially enhancing anti-tumor immunity.

Regulatory T cells (Tregs) are a specialized subset of T cells that play a pivotal role in establishing an immunosuppressive microenvironment. The infiltration of Tregs is closely associated with HCC progression and poor prognosis [38]. As shown in Fig. 7C and D, compared to the control group, blank GLPs treatment resulted in a reduction in Treg cells. Notably, IR780 GLPs significantly decreased the Treg population compared to both the control and IR780 LPs groups. In contrast, the free drug formulations exhibited the least effect on Treg modulation. These findings suggest that IR780 GLPs effectively downregulate Tregs, contributing to the reprogramming of the immunosuppressive tumor microenvironment and potentially enhancing anti-tumor immunity.

To assess immune activation following tumor microenvironment remodeling, we quantified infiltrating $CD3^+$ T, $CD4^+$ T, and $CD8^+$ T cells (Fig. 7E–H). Compared to the saline group, all treatment groups exhibited a significant increase in the total infiltration of $CD3^+$ T cells, with the IR780 GLPs group showing the most prominent effect. The proportion of $CD3^+$ T cells in this group was 3.69 times higher than that the control group. Additionally, IR780 GLPs demonstrated a 3.52-fold increase in the proportion of $CD8^+$ T cells compared to the control group, and a 1.95-fold increase compared to the IR780 LPs group. These results suggest that GL, as a carrier for IR780, significantly improves the tumor immune-suppressive microenvironment, activates immune responses, and enhances the infiltration of cytotoxic T lymphocytes, thereby supporting IR780-mediated tumor eradication.

To further investigate the immune status of the tumor after treatment, we measured serum levels of relevant cytokines. As shown in Fig. 7I–M, compared to the saline group, both IR780 LPs and IR780 GLPs significantly suppressed the proliferation of TGF-β. However, compared to IR780 LPs, IR780 GLPs demonstrated a more pronounced downregulation of TGF-β, which can be attributed to the ability of glycyrrhizin to improve the immunosuppressive microenvironment. Additionally, we found that IR780 GLPs significantly decreased IL-10, while significantly upregulating IL-12 levels. Furthermore, TNF-α and IFN-γ, which are typically considered key indicators of cellular immune activation, were significantly elevated in the IR780 GLPs group compared to other treatment groups. These findings suggest that IR780 GLPs can activate cellular immunity by remodeling the tumor immunosuppressive microenvironment, thereby enhancing anti-cancer efficacy.

To assess the safety of IR780 GLPs, we collected the main organs (heart, liver, spleen, lungs, and kidneys) from H22 tumor-bearing mice for H&E staining. As shown in Fig. 8, there were no significant differences were observed in H&E staining between the treatment groups and the saline group. No apparent lesions or damage were detected in any of the organs, indicating that IR780 GLPs exhibited good safety under the administered dosing regimen.

4. Conclusion

In this study, to overcome the limitations of phototherapy in HCC, including HSP90-mediated thermal resistance, immunosuppressive tumor microenvironment, and poor delivery efficiency of photosensitizers, we developed a novel GL-based lipid nanoparticle system for encapsulating IR780. This platform significantly enhanced the synergistic efficacy of PTT and chemotherapy. The IR780 GLPs exhibited excellent photothermal and photodynamic properties, efficient drug release, and enhanced cellular uptake, resulting in increased cytotoxicity and apoptosis in tumor cells. Upon NIR irradiation, IR780 GLPs effectively suppressed HSP90 expression, thereby improving photothermal efficiency. Furthermore, the nanoparticles demonstrated strong

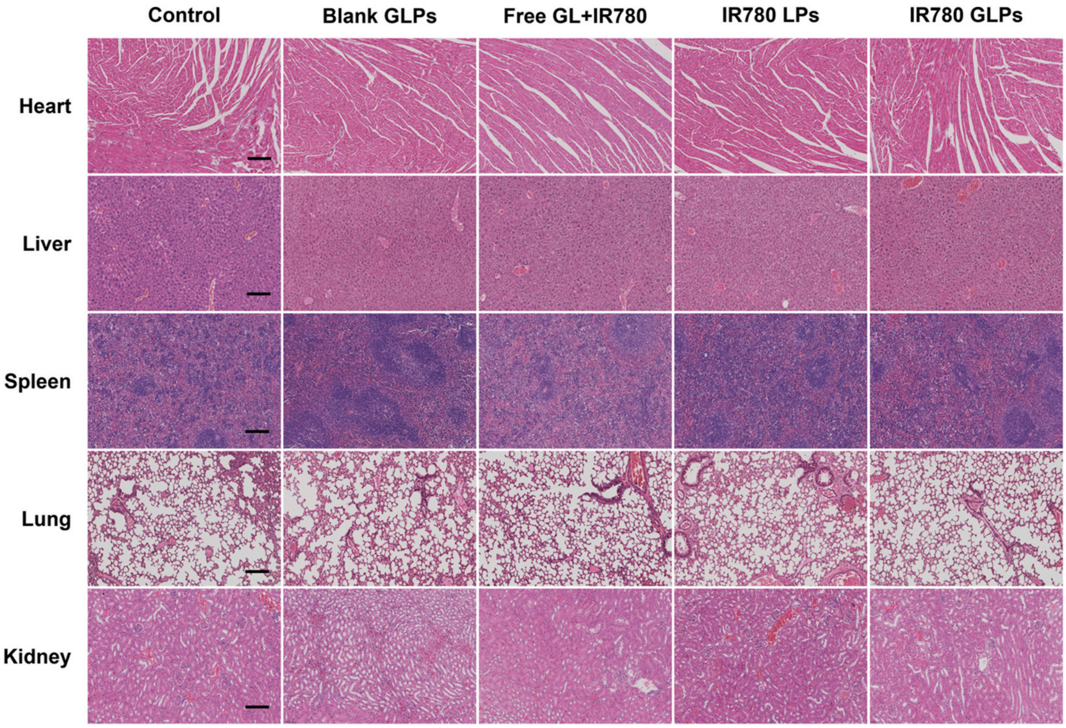

Fig. 8. H&E staining of major organs to evaluate biosafety of IR780 GLPs. The scale bar represents 50 μm.

hepatic tumor-targeting capacity and reprogrammed the tumor immune microenvironment by reducing regulatory T cells, repolarizing M2 macrophages to the M1 phenotype, and promoting $CD8^+$ T cell infiltration. These combined effects contribute to a robust and comprehensive antitumor response, offering a promising strategy for improved HCC treatment.

CRediT authorship contribution statement

Yihan Wu: Writing – original draft, Funding acquisition. **Chenglin He:** Methodology. **Yu Huang:** Writing – review & editing. **Zhen Liu:** Formal analysis. **Ying Zhu:** Software. **Manyin Zhang:** Resources. **Jingjing Li:** Data curation. **Yu You:** Validation. **Yitao Wang:** Visualization. **Tao Chen:** Methodology. **Jinming Zhang:** Supervision, Funding acquisition.

Declaration of competing interest

The authors declare that they have no known competing financial interests or personal relationships that could have appeared to influence the work reported in this paper.

Acknowledgments

This work was supported by funding from the Multi disciplinary Evaluation of Southwest Characteristic TCM Resources Multidisciplinary Interdisciplinary Innovation Team (No. ZYYCXTD-D-202209, China). International Science and Technology Innovation Cooperation Project of Sichuan Provincial Department of Science and Technology (No. 2023ZYD0052). Technical Development Special Project of Sichuan Province (No.2024YFHZ0360). China Postdoctoral Science Foundation (No: GZC20230335). Natural Science Foundation of Sichuan Province of China for Youths (No. 25QNJJ4735), Joint Innovation Fund Project of Chengdu University of Traditional Chinese Medicine and Hospital (No. LH202402038).

Appendix A. Supplementary data

Supplementary data to this article can be found online at https://doi.org/10.1016/j.mtbio.2025.102353.

Data availability

Data will be made available on request.

References

[1] Y. Cai, T. Chai, W. Nguyen, J. Liu, E. Xiao, X. Ran, Y. Ran, D. Du, W. Chen, X. Chen, Phototherapy in cancer treatment: strategies and challenges, Signal Transduct. Targeted Ther. 10 (2025) 115, https://doi.org/10.1038/s41392-025-02140-y.

[2] Y. Wang, K. Ma, M. Kang, D. Yan, N. Niu, S. Yan, P. Sun, L. Zhang, L. Sun, D. Wang, H. Tan, B.Z. Tang, A new era of cancer phototherapy: mechanisms and applications, Chem. Soc. Rev. 53 (2024) 12014–12042, https://doi.org/10.1039/d4cs00708e.

[3] Z. Cao, J. Liu, X. Yang, Deformable nanocarriers for enhanced drug delivery and cancer therapy, Explorations 4 (2024) 20230037, https://doi.org/10.1002/EXP.20230037.

[4] M.C.P. Fialho, M.A. De Oliveira, M.G.C. Machado, C.M. Lacerda, V.C.F.J.J.o. N. Mosqueira, IR780-Based Nanotheranostics and in Vivo Effects: A Review, vol. 6, 2025, https://doi.org/10.3390/jnt6010008.

[5] Z. Yang, J. Wang, S. Liu, X. Li, L. Miao, B. Yang, C. Zhang, J. He, S. Ai, W. Guan, Defeating relapsed and refractory malignancies through a nano-enabled mitochondria-mediated respiratory inhibition and damage pathway, Biomaterials 229 (2020) 119580, https://doi.org/10.1016/j.biomaterials.2019.119580.

[6] J. Yan, X. Ma, D. Liang, M. Ran, D. Zheng, X. Chen, S. Zhou, W. Sun, X. Shen, H. Zhang, An autocatalytic multicomponent DNAzyme nanomachine for tumor-specific photothermal therapy sensitization in pancreatic cancer, Nat. Commun. 14 (2023) 6905, https://doi.org/10.1038/s41467-023-42740-2.

[7] X. Li, J.F. Lovell, J. Yoon, X. Chen, Clinical development and potential of photothermal and photodynamic therapies for cancer, Nat. Rev. Clin. Oncol. 17 (2020) 657–674, https://doi.org/10.1038/s41571-020-0410-2.

[8] S. Zhou, H. Tian, J. Yan, Z. Zhang, G. Wang, X. Yu, W. Sang, B. Li, G. Spmok, J.J.C. C.L. Song, IR780/Gemcitabine-conjugated Metal-Phenolic Network Enhanced Photodynamic Cancer Therapy, vol. 35, 2024, pp. 305–309, https://doi.org/10.1016/j.cclet.2023.108312.

[9] J. Ma, N. Li, J. Wang, Z. Liu, Y. Han, Y. Zeng, In vivo synergistic tumor therapies based on copper sulfide photothermal therapeutic nanoplatforms, Explorations 3 (2023) 20220161, https://doi.org/10.1002/EXP.20220161.

[10] D. Jiang, C. Chen, P. Dai, C. Li, Z. Feng, N. Dong, F. Wu, J. Xu, P. Wu, L. Chu, S. Li, X. Li, Y. Yang, W. Zhang, Z. Wang, Deep near infrared light-excited stable synergistic photodynamic and photothermal therapies based on P-IR890 nano-photosensitizer constructed via a non-cyanine dye, Asian J. Pharm. Sci. 19 (2024) 100955, https://doi.org/10.1016/j.ajps.2024.100955.

[11] S. Luo, Y. Wang, S. Shen, P. Tang, Z. Liu, S. Zhang, D. Wu, IR780-Loaded Hyaluronic Acid@Gossypol–Fe(III)–EGCG Infinite Coordination Polymer Nanoparticles for Highly Efficient Tumor Photothermal/Coordinated Dual Drugs Synergistic Therapy, Adv. Funct. Mater. https://doi.org/10.1002/adfm.202100954.

[12] W. Zhang, X.F. Du, B. Liu, C. Li, J. Long, M.X. Zhao, Z. Yao, X.J. Liang, Y. Lai, Engineering supramolecular Nanomedicine for targeted near infrared-triggered mitochondrial Dysfunction to potentiate cisplatin for efficient Chemophototherapy, ACS Nano 16 (2022) 1421–1435, https://doi.org/10.1021/acsnano.1c09555.

[13] T.Y. Lin, W. Guo, Q. Long, A. Ma, Q. Liu, H. Zhang, Y. Huang, S. Chandrasekaran, C. Pan, K.S. Lam, Y. Li, HSP90 inhibitor encapsulated Photo-Theranostic nanoparticles for synergistic combination cancer therapy, Theranostics 6 (2016) 1324–1335, https://doi.org/10.7150/thno.14882.

[14] M. Overchuk, R.A. Weersink, B.C. Wilson, G. Zheng, Photodynamic and photothermal therapies: synergy Opportunities for Nanomedicine, ACS Nano 17 (2023) 7979–8003, https://doi.org/10.1021/acsnano.3c00891.

[15] B. Tian, C. Wang, Y. Du, S. Dong, L. Feng, B. Liu, S. Liu, H. Ding, S. Gai, F. He, P. Yang, Near infrared-triggered Theranostic nanoplatform with controlled release of HSP90 inhibitor for synergistic mild photothermal and enhanced Nanocatalytic therapy with hypoxia relief, Small 18 (2022) e2200786, https://doi.org/10.1002/smll.202270147.

[16] R. Li, X. Hu, F. Shang, W. Wu, H. Zhang, Y. Wang, J. Pan, S. Shi, C. Dong, Treatment of triple negative breast cancer by near infrared light triggered mild-temperature photothermal therapy combined with oxygen-independent cytotoxic free radicals, Acta Biomater. 148 (2022) 218–229, https://doi.org/10.1016/j.actbio.2022.06.011.

[17] T. Zhang, B. Wu, O.U. Akakuru, C. Yao, S. Sun, L. Chen, W. Ren, A. Wu, P. Huang, Hsp90 inhibitor-loaded IR780 micelles for mitochondria-targeted mild-temperature photothermal therapy in xenograft models of human breast cancer, Cancer Lett. 500 (2021) 41–50, https://doi.org/10.1016/j.canlet.2020.12.028.

[18] Y. Tang, H.K. Bisoyi, X.M. Chen, Z. Liu, X. Chen, S. Zhang, Q. Li, Pyroptosis-mediated synergistic photodynamic and photothermal immunotherapy enabled by a tumor-membrane-targeted photosensitive dimer, Adv. Mater. 35 (2023) e2300232, https://doi.org/10.1002/adma.202300232.

[19] J. Huang, X. Leng, T. Jiang, L. Xu, J. Zheng, M. Fang, J. Wang, Z. Wang, L. Zhang, Oxygen-carrying nanoplatform to reprogram tumor immunosuppressive microenvironment and enhance photothermal-immunotherapy, Mater. Today Bio 19 (2023) 100555, https://doi.org/10.1016/j.mtbio.2023.100555.

[20] K.F. Xu, S.Y. Wu, Z. Wang, Y. Guo, Y.X. Zhu, C. Li, B.H. Shan, X. Zhang, X. Liu, F. G. Wu, Hyperbaric oxygen enhances tumor penetration and accumulation of engineered bacteria for synergistic photothermal immunotherapy, Nat. Commun. 15 (2024) 5147, https://doi.org/10.1038/s41467-024-49156-6.

[21] G. Zhang, W. Cheng, L. Du, C. Xu, J. Li, Synergy of hypoxia relief and heat shock protein inhibition for phototherapy enhancement, J. Nanobiotechnol. 19 (2021) 9, https://doi.org/10.1186/s12951-020-00749-5.

[22] P. Xiong, X. Wei, L. Zhou, W. Zhou, M. Li, Y. Ge, J. Zou, S. Peng, L. Jiang, L.J.A.F. M. Tian, Near-infrared light-triggered MXene Nanocomposite for tumor-specific mild photothermal-enhanced Chemodynamic therapy, Adv. Funct. Mater. 34 (2024), https://doi.org/10.1002/adfm.202405124.

[23] G. Yang, T. Song, H. Zhang, M. Li, X. Wei, W. Zhou, C. Wu, Y. Liu, H. Yang, Stimulus-detonated Biomimetic "Nanobomb" with controlled release of HSP90 inhibitor to Disrupt mitochondrial function for synergistic gas and photothermal therapy, Adv. Healthcare Mater. 12 (2023), https://doi.org/10.1002/adhm.202300945.

[24] G. Pastorino, L. Cornara, S. Soares, F. Rodrigues, M. Oliveira, Liquorice (Glycyrrhiza glabra): a phytochemical and pharmacological review, Phytother Res. : PTR 32 (2018) 2323–2339, https://doi.org/10.1002/ptr.6178.

[25] X. Sha, C. Wang, Y. Liu, N. Zhong, Y. Lu, Q. Zhang, S. Lu, D. He, Y. Jin, Y. Tang, S. Wang, Multifunctional glycyrrhizic acid-loaded nanoplatform combining ferroptosis induction and HMGB1 blockade for enhanced tumor immunotherapy, J. Nanobiotechnol. 23 (2025) 224, https://doi.org/10.1186/s12951-025-03307-z.

[26] M. Xiao, Z. Guo, Y. Yang, C. Hu, Q. Cheng, C. Zhang, Y. Wu, Y. Cheng, W.L. M. Benson, S.M.N. Shamay, G.P. Leung, J. Li, H. Gao, J. Zhang, Glycyrrhizic acid-based multifunctional nanoplatform for tumor microenvironment regulation, Chin. J. Nat. Med. 22 (2024) 1089–1099, https://doi.org/10.1016/S1875-5364(24)60685-0.

[27] J. Cui, X. Wang, J. Li, A. Zhu, Y. Du, W. Zeng, Y. Guo, L. Di, R. Wang, Immune Exosomes loading Self-Assembled Nanomicelles traverse the blood-brain barrier for chemo-immunotherapy against glioblastoma, ACS Nano (2023), https://doi.org/10.1021/acsnano.2c10219.

[28] L. Zhang, J. Lu, Combination strategies for first-line treatment of patients with unresectable hepatocellular carcinoma: prospect of natural products, Chin. J. Nat. Med. 22 (2024) 1–3, https://doi.org/10.1016/S1875-5364(24)60574-1.

[29] Q.S. Wang, L.N. Gao, X.N. Zhu, Y. Zhang, C.N. Zhang, D. Xu, Y.L. Cui, Co-delivery of glycyrrhizin and doxorubicin by alginate nanogel particles attenuates the activation of macrophage and enhances the therapeutic efficacy for hepatocellular carcinoma, Theranostics 9 (2019) 6239–6255, https://doi.org/10.7150/thno.35972.

[30] Z. Xu, Y. Huang, Y. Wu, J. Chen, S.W. Seto, G.P. Leung, Y. Cai, J. Li, J. Zhang, Glycyrrhizic acid-lipid framework nanovehicle loading triptolide for combined immunochemotherapy, ACS Appl. Mater. Interfaces 15 (2023) 41337–41350, https://doi.org/10.1021/acsami.3c08003.

[31] L. Su, Y. Zhu, X. Li, D. Wang, X. Chen, Z. Liu, J. Li, C. Zhang, J. Zhang, Topical adhesive spatio-temporal nanosystem co-delivering chlorin e6 and HMGB1 inhibitor glycyrrhizic acid for in situ psoriasis chemo-phototherapy, Acta Pharm. Sin. B 15 (2025) 1126–1142, https://doi.org/10.1016/j.apsb.2024.12.020.

[32] H. Tian, T. Zhang, S. Qin, Z. Huang, L. Zhou, J. Shi, E.C. Nice, N. Xie, C. Huang, Z. Shen, Enhancing the therapeutic efficacy of nanoparticles for cancer treatment using versatile targeted strategies, J. Hematol. Oncol. 15 (2022) 132, https://doi.org/10.1186/s13045-022-01320-5.

[33] Z. Xie, Y. Zhai, Y. Zhang, M. He, X. Wang, S. Yu, H. Xiao, Y.J.J.o.F.F. Song, Antioxidant and anti-HepG2 cell activities of a novel bioactive peptide from cowhide collagen in vitro, Journal of Future Foods 4 (2024) 248–257, https://doi.org/10.1016/j.jfutfo.2023.07.007.

[34] Q. Yang, N. Guo, Y. Zhou, J. Chen, Q. Wei, M. Han, The role of tumor-associated macrophages (TAMs) in tumor progression and relevant advance in targeted therapy, Acta Pharm. Sin. B 10 (2020) 2156–2170, https://doi.org/10.1016/j.apsb.2020.04.004.

[35] J. Bruggisser, B. Tarek, M. Wyder, P. Müller, C. von Ballmoos, G. Witz, G. Enzmann, U. Deutsch, B. Engelhardt, H. Posthaus, CD31 (PECAM-1) serves as the endothelial cell-specific receptor of Clostridium perfringens β-toxin, Cell Host Microbe 28 (2020) 69–78.e66, https://doi.org/10.1016/j.chom.2020.05.003.

[36] W. Lu, J. Zhao, X. Cai, Y. Wang, W. Lin, Y. Fang, Y. Wang, J. Ao, J. Shou, J. Xu, Cadherin-responsive hydrogel combined with dental pulp stem cells and fibroblast growth factor 21 promotes diabetic scald repair via regulating epithelial-mesenchymal transition and necroptosis, Mater. Today Bio 24 (2024), https://doi.org/10.1016/j.mtbio.2023.100919.

[37] J. Cheng, Y. Zhu, Y. Dai, L. Li, M. Zhang, D. Jin, M. Liu, J. Yu, W. Yu, D. Su, J. Zou, X. Chen, Y. Liu, Gas-mediated tumor energy remodeling for sensitizing mild photothermal therapy, Angew. Chem. 62 (2023), https://doi.org/10.1002/anie.202304312.

[38] C. Tay, A. Tanaka, S. Sakaguchi, Tumor-infiltrating regulatory T cells as targets of cancer immunotherapy, Cancer Cell 41 (2023) 450–465, https://doi.org/10.1016/j.ccell.2023.02.014.